

# PEPSI deep spectra

## II. *Gaia* benchmark stars and other M-K standards<sup>★</sup>

K. G. Strassmeier, I. Ilyin, and M. Weber

Leibniz-Institute for Astrophysics Potsdam (AIP), An der Sternwarte 16, 14482 Potsdam, Germany  
e-mail: kstrassmeier@aip.de; ilyin@aip.de; mweber@aip.de

Received 24 July 2017 / Accepted 22 November 2017

### ABSTRACT

**Context.** High-resolution échelle spectra confine many essential stellar parameters once the data reach a quality appropriate to constrain the various physical processes that form these spectra.

**Aims.** We provide a homogeneous library of high-resolution, high-S/N spectra for 48 bright AFGKM stars, some of them approaching the quality of solar-flux spectra. Our sample includes the northern *Gaia* benchmark stars, some solar analogs, and some other bright Morgan-Keenan (M-K) spectral standards.

**Methods.** Well-exposed deep spectra were created by average-combining individual exposures. The data-reduction process relies on adaptive selection of parameters by using statistical inference and robust estimators. We employed spectrum synthesis techniques and statistics tools in order to characterize the spectra and give a first quick look at some of the science cases possible.

**Results.** With an average spectral resolution of  $R \approx 220\,000$  ( $1.36 \text{ km s}^{-1}$ ), a continuous wavelength coverage from 383 nm to 912 nm, and S/N of between 70:1 for the faintest star in the extreme blue and 6000:1 for the brightest star in the red, these spectra are now made public for further data mining and analysis. Preliminary results include new stellar parameters for 70 Vir and  $\alpha$  Tau, the detection of the rare-earth element dysprosium and the heavy elements uranium, thorium and neodymium in several RGB stars, and the use of the  $^{12}\text{C}$  to  $^{13}\text{C}$  isotope ratio for age-related determinations. We also found Arcturus to exhibit few-percent Ca II H&K and H $\alpha$  residual profile changes with respect to the KPNO atlas taken in 1999.

**Key words.** stars: atmospheres – stars: late-type – stars: abundances – stars: activity – stars: fundamental parameters

### 1. Introduction

High-resolution spectroscopy is key for progress in many fields of astrophysics, most obviously for fundamental stellar physics. The advent of ESA's *Gaia* mission spurred a large high-spectral-resolution survey of FGK-type stars at ESO with significant results now coming online (e.g., Smiljanic et al. 2014). This survey, dubbed the *Gaia*-ESO survey (Gilmore et al. 2012), also defined a list of 34 benchmark FGK stars in both hemispheres (Blanco-Cuaresma et al. 2014) that were analyzed with many different spectrum-synthesis codes and with data from different spectrographs. The analysis focused, among other topics, on global stellar parameters like effective temperatures and gravities (Heiter et al. 2015), metallicity (Jofré et al. 2014) and chemical abundances (Jofré et al. 2015), and on some stars in detail (e.g., Creevey et al. 2015 on HD 140283). A recent addition to low-metallicity stars was presented by Hawkins et al. (2016).

One of the major conclusions from this program is that even for main sequence stars the spectroscopically determined

quantities may differ significantly with respect to the fundamental value obtained from direct radius and flux measurements. But even within the spectroscopic analyzes the global parameters  $T_{\text{eff}}$ ,  $\log g$ , and metallicity, along with micro- and macroturbulence and rotational line broadening, differ uncomfortably large (see, for example the discussion in Heiter et al. 2015). Among the least cooperative stars appear to be the giants and metal-poor dwarfs. Comparisons indicate, for example that for solar-metallicity giants with  $T_{\text{eff}} \approx 5000 \text{ K}$  and  $\log g \approx 2.8$ , the spectroscopic approach can lead to overestimated gravities. Intrinsic line-profile variability may become the limit for precision, in particular due to (non-detected) p-mode oscillations for the K giants and rotationally-modulated stellar activity (spots, faculae, etc.) for all of the cool stars. Besides intrinsic stellar variability, one extra source of uncertainty is the remaining blending situation with weak molecular lines due to finite spectral resolution.

The data in the *Gaia* benchmark spectral library provided by Blanco-Cuaresma et al. (2014) were originally homogenized to the highest minimum spectral resolution of the different spectrographs involved, and corresponded in practice to  $R = \lambda/\Delta\lambda = 70\,000$ . The vast majority of the spectra for the benchmarks are from HARPS (Mayor et al. 2003) with an original resolution of 115 000. NARVAL spectra (Aurière 2003) have an average resolution of 65 000 (Paletou et al. 2015), and the UVES data (Dekker et al. 2000) have 78 000–115 000. Peak signal-to-noise ratios (S/N) of between 150 to 824 were achieved. Higher S/N was obtained for eight bright stars in the UVES-POP library (Bagnulo et al. 2003) but with the lower spectral resolution of  $\approx 80\,000$ . Yet, if some of the most decisive

<sup>★</sup> Based on data acquired with PEPSI using the Large Binocular Telescope (LBT) and the Vatican Advanced Technology Telescope (VATT). The LBT is an international collaboration among institutions in the United States, Italy, and Germany. LBT Corporation partners are the University of Arizona on behalf of the Arizona university system; Istituto Nazionale di Astrofisica, Italy; LBT Beteiligungsgesellschaft, Germany, representing the Max-Planck Society, the Leibniz-Institute for Astrophysics Potsdam (AIP), and Heidelberg University; the Ohio State University; and the Research Corporation, on behalf of the University of Notre Dame, University of Minnesota and University of Virginia.

astrophysical processes for stellar variability, that is, stellar convection, is to be detected and characterized in spectra, it requires much higher spectral resolution and even higher S/N, and thus even larger telescopes. Most of the stars analyzed in work previous to the *Gaia*-ESO survey had even lower resolution than the minimum resolution for the benchmark stars, for example the bright M-giant  $\gamma$  Sge with 50–60 000, which is still the typical spectral resolution for a fixed-format échelle spectrograph on a smaller telescope.

We have just put into operation the optical high-resolution échelle spectrograph PEPSI (Potsdam Echelle Polarimetric and Spectroscopic Instrument) at the currently largest aperture optical telescope in the world; the effective 11.8 m Large Binocular Telescope (LBT; Hill et al. 2012). PEPSI provides a spectral resolution of up to 270 000 for the wavelength range 383–912 nm and can alternatively be fed by the nearby 1.8 m Vatican Advanced Technology Telescope (VATT) or by a small solar disk integration (SDI) telescope. The instrument is described in detail in Strassmeier et al. (2015) and we refer to this paper for technical and operational details. Solar flux spectra with PEPSI were presented and analyzed in paper I (Strassmeier et al. 2018), where we also described the data reduction in more detail. A further application is presented in paper III to Kepler-444 (Mack et al. 2018).

The current paper presents first PEPSI spectra for 48 bright stars including those of the original 34 *Gaia* benchmark stars that were observable from the northern LBT site. Data were taken during several instrument commissioning runs throughout 2015 until March 2017. Peak S/N of several thousand in the red wavelength regions were achieved with average-combining individual exposures. All these spectra are extremely rich in detail and therefore are made public for further data mining and analysis. Science-ready FITS files of the average-combined spectra are available for download<sup>1</sup> and raw data may be requested. Section 2 describes the observations and the spectrograph while Sect. 3 briefly reiterates the data reduction. Section 4 gives a first quality assessment of the data product. The stellar sample and its science cases with a few additions to the original *Gaia* benchmark stars are discussed in Sects. 5 and 6, respectively. Section 7 is a summary.

## 2. Observations

High-resolution spectra with  $R = \lambda/\Delta\lambda$  between 200 000 and up to 270 000 were obtained with PEPSI (Strassmeier et al. 2015) at the  $2 \times 8.4$  m LBT (Hill et al. 2012). PEPSI is a fiber-fed white-pupil échelle spectrograph with two arms (blue and red optimized) covering the wavelength range 383–912 nm with six different cross dispersers (CD). The instrument is stabilized in a pressure and thermally controlled chamber and is fed by three pairs of octagonal fibers per LBT unit telescope (named SX and DX). The different core diameters of the fibers and their respective image slicers set the three different resolutions of the spectrograph (43 000, 120 000 and 250 000). In use for this paper was image slicer block #2. Its 250 000-mode, which was used for the spectra in this paper, is made possible with the seven-slice image slicers and a 100- $\mu$ m fiber with a projected sky aperture of 0.74'', comparable to the median seeing of the LBT site. Its resolution element is sampled with two pixels. One resolution element corresponds to  $1.2 \text{ km s}^{-1}$  for the resolving power of 250 000. Two  $10.3 \text{ k} \times 10.3 \text{ k}$  STA1600LN CCDs with 9- $\mu$ m pixels record a

total of 92 échelle orders in six wavelength settings. The dispersion changes from 8 mÅ/pixel at 400 nm to 18 mÅ/pixel at 900 nm and results in a  $\approx 430\,000$  pixel long spectrum with unequally spaced step size. An example spectrum is shown in Fig. 1.

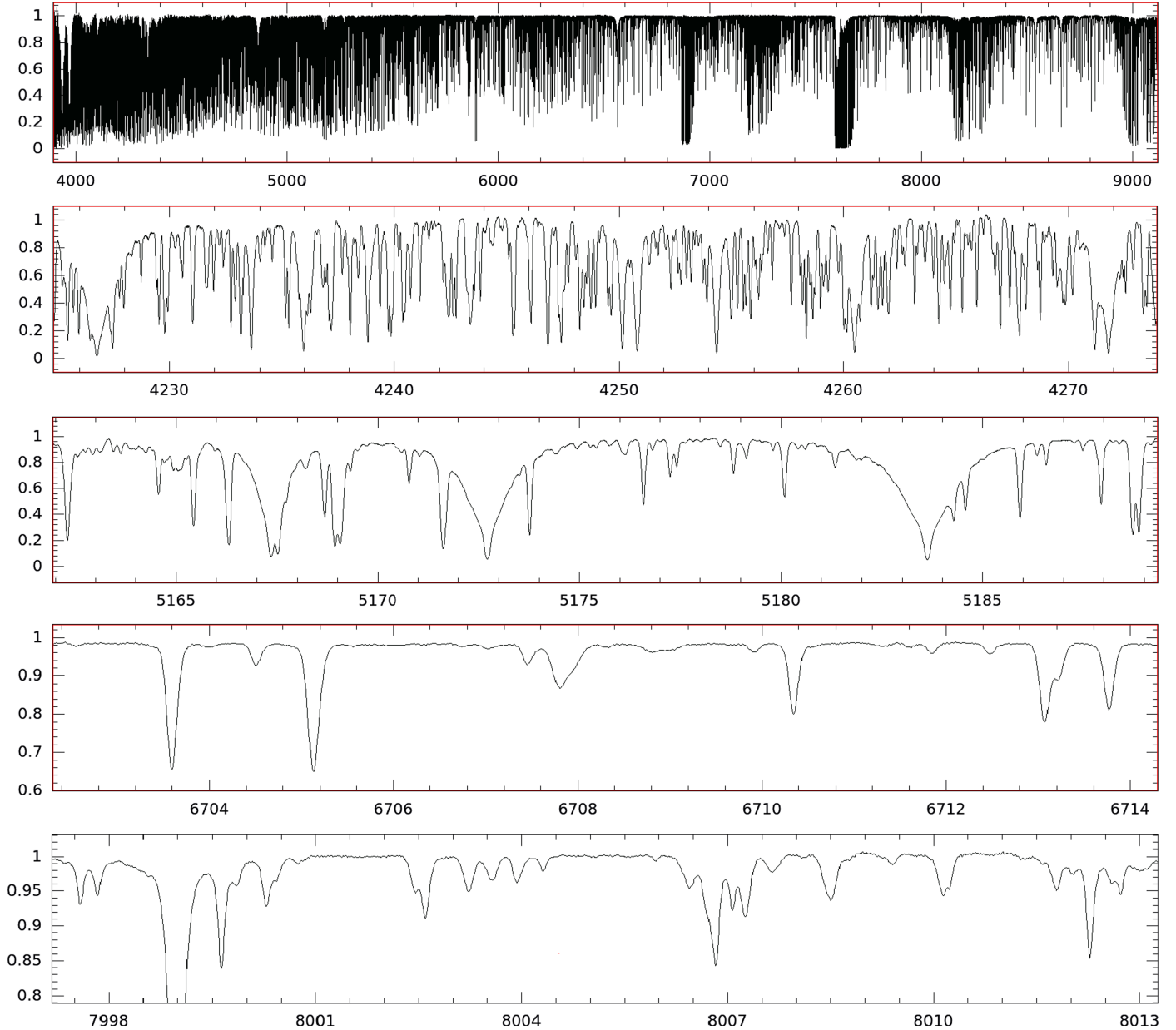
The six wavelength settings are defined by the six cross dispersers (CD I to VI), three per arm and two always simultaneously. It takes three exposures to cover the entire wavelength range 383–912 nm. Several of the spectra extend out to 914 nm because we repositioned cross disperser VI during commissioning and then gained another échelle order. Any of the three resolution modes can be used either with sky fibers for simultaneous sky and target exposures or with light from a stabilized Fabry–Pérot etalon (FPE) for simultaneous fringe and target exposures for precise radial velocities (RV). However, the short integrations for the targets in this paper made the use of the sky fibers obsolete. Therefore, all spectra in this paper were taken in target+target mode, i.e., without simultaneous sky or FPE exposures, leaving two simultaneous target spectra on the CCD (one from each of the 8.4 m LBT unit telescopes). We always refer to the combined target+target spectrum when referring to “an LBT spectrum”, e.g. for example in the number of spectra in the tables. The SDI telescope makes use of PEPSI during day time and also consists of two spectra per exposure. Paper I in this series dealt with these spectra. A 450-m fiber feed (Sablowski et al. 2016) from the 1.8 m VATT was used for very bright stars on several occasions. We note that the VATT spectra consist of just a single target spectrum on the CCD because it is only a single telescope.

Table A.1 summarizes the detailed observing log and identifies the individual spectra. Observations with the LBT were conducted during the epochs April 1–2 and 8–10, May 23–25, September 25 and 27, and November 19, in 2015; during June 2–4 and September 29–30 in 2016; and on March 3, 2017. Observations with the VATT were done during the epochs April 1–7, May 1–10, May 26–June 1, June 17–24, in 2015, and April 2–9 and May 24–June 2 in 2016. At around mid November 2015 the Blue CCD developed a bad amplifier (amp #5) affecting a section of  $5000 \times 1280$  pixels on the CCD. It resulted in a drastically degraded quantum efficiency and practically in a loss of the three halves of the respective échelle orders that fell on this CCD section. This was repaired in early 2016 and the affected wavelength region was re-observed for some of the stars (but at a grossly different epoch). The spectrograph was in different states of alignment and focus and thus resulted in slightly different dependencies of spectral resolution vs wavelength. Also, acceptable barometric stability of the chamber was not achieved until summer 2015.

## 3. Data reduction

PEPSI data reduction was described in detail in paper I. The Sun is the only target where we can compare to even higher quality data from Fourier Transform Spectrographs (e.g., Wallace et al. 2011; Reiners et al. 2016). The stellar PEPSI data in the present paper do not differ principally from the solar PEPSI data except for the S/N. This allows a direct comparison of solar flux spectra with stellar spectra because the solar light passes through exactly the same optical path as the stellar light. A full-wavelength PEPSI exposure in the  $R = 250\,000$  mode is always merged from seven (image) slices per échelle order, 17 échelle orders per cross disperser, and two arms recorded with two different CCDs optimized for blue and red response.

<sup>1</sup> <https://pepsi.aip.de>



**Fig. 1.** Example spectrum of 70 Vir, spectral type G4 V–IV (*x*-axis is wavelength in Angstrom, *y*-axis is relative intensity). *Top*: full 5290-Å wavelength coverage. The other panels show magnifications of four selected wavelength regions. *Top down*: numerous Fe I lines around 4250 Å, the Mg I triplet at 5175 Å, the Li I 6708-Å region, and the 8004-Å line region commonly used for  $^{12}\text{C}/^{13}\text{C}$  determination.

The data were reduced with the Spectroscopic Data System for PEPSI (SDS4PEPSI) which is a generic software package written in C++ under a Linux environment and loosely based upon the 4A software (Ilyin 2000) developed for the SOFIN spectrograph at the Nordic Optical Telescope. It relies on adaptive selection of parameters by using statistical inference and robust estimators. The standard reduction steps include bias overscan detection and subtraction, scattered light surface extraction from the inter-order space and subtraction, definition of échelle orders, optimal extraction of spectral orders, wavelength calibration, and a self-consistent continuum fit to the full 2D image of extracted orders. Every target exposure is made with a simultaneous recording of the light from a Fabry–Pérot etalon through the sky fibers. For the spectra in this paper, the Fabry–Pérot wavelength solution was not implemented.

Instead, exposures with a standard Thorium–Argon (Th–Ar) hollow-cathode lamp were used for the wavelength calibration. Its solution is based on about 5000 spectral lines from all seven image slices and all spectral orders. A 3D Chebychev polynomial fit achieves an accuracy of about 3–5  $\text{m s}^{-1}$  in the image center with a rms of about 50  $\text{m s}^{-1}$  across the entire CCD. The Th–Ar calibration images are taken during daytime before the observing night and the wavelength scale zero point of the science images is thus relying on the stability of the PEPSI chamber. Wavelengths in this paper are given for air and radial velocities are reduced to the barycentric motion of the solar system. We note that the spectra in the present paper were reduced and extracted just like the Sun-as-a-star data in paper I with the only difference that the continuum normalization was adjusted to the spectral classification.

In order to achieve the high S/N, we employ a “super master” flat-fielding procedure that is based on a combined flat-field image made from  $\approx 2000$  individual images taken during daytime. Individual stellar spectra are first flat fielded, then extracted, and then average combined with a  $\chi^2$  minimization procedure weighted with the inverse variance in each CCD pixel. For three taps on the STA1600LN CCDs surface, the pixel response is a function of the exposure level. This blemish is dubbed fixed-pattern noise and described in detail in paper I. In order to achieve very high S/N, all raw images are corrected for nonlinearity of each CCD pixel vs its ADU level with the use of the super master flat field image. It comprises a polynomial fit of the CCD fixed-pattern response function in 70 de-focused flat field images at different exposure levels. Each of such an image is again the sum of 70 individual exposures made in order to minimize the photon noise. The fixed-pattern response function is the ratio of the flat field image and its 2D smoothed spline fit which removes all signatures of the de-focused spectral orders. The accuracy of this correction allows reaching a S/N in the combined spectra of as high as 4500. Because the pattern shows a spatial periodicity with a spacing of 38 pixels, which is wavelength dependent on the red CCD (but not on the blue CCD), it leaves residual ripples with a periodicity of 38 pixels in the spectrum. It is being removed to the best possible level but the residual pixel-to-pixel non uniformity after the super master flat division currently limits the effective S/N from the affected CCD taps to  $\approx 1300:1$ . Other regions are unaffected.

## 4. Data product

### 4.1. Building deep spectra

Deep spectra in this paper are built by average-combining individual spectra, usually taken back-to-back within a single night. For some targets individual spectra are from different nights or even different runs. The observing log is given in Table A.1. Any spectrum co-addition is prone to variations of the entire spectrograph system, including errors from the seeing-dependent fiber injection or the temperature-sensitive CCD response or the optical-path differences due to the LBT being two telescopes and/or when using the VATT as the light feed.

When two spectra from different LBT sides are combined, the spectra are re-sampled into the wavelength grid of the first spectrum, then they are averaged with their corresponding weights (inverse variance in each pixel). First, the optimally extracted spectra from every slice of the image slicer are combined into a single spectrum for each spectral order. Prior to its averaging, all spectra are re-sampled into the common wavelength grid of the middle slice. The wavelength in each pixel is defined by the Th-Ar wavelength solution and remains unequally sampled. Then, the two average spectra from the two sides of the LBT telescope are combined into a single spectrum with the weighted average to the common wavelength grid of the first spectrum. One spectrum is re-sampled to the other by means of spline interpolation.

Because the spectra are normalized to a pseudo-continuum  $I/I_c$ , there is no need to re-scale them in intensity and the final continuum level will be adherent to the one with the higher S/N. The very same procedure is applied for building the average-combined deep spectra. For more details we refer to paper I.

### 4.2. Intrinsic spectrum variations

A deep spectrum may be affected by intrinsic stellar changes, for example due to rotational modulation by spots and plages, non-radial surface oscillations, or Doppler wobbling due to unseen stellar companions or exoplanets. However, exposure times are usually rather short compared to the typical stellar variability timescales. When using the LBT the exposure times are typically just tens of seconds up to a few minutes but exposure times with the VATT and its 450-m fiber link can be up to 60 min. Nevertheless, even after adding the CCD read-out overhead of 90 s and the co-adding of, say, typically four spectra, the total time on target still sums up to a relatively short period in time, typically just tens of minutes for the LBT data and up to a maximum of 3 h for the VATT targets. Any intrinsic changes with a timescale significantly longer than this we can safely dub non critical. This is certainly the case for rotational modulation and the revolution of orbital companions where we expect periods in excess of many days up to thousands of days. An example is  $\alpha$  Tau, which shows RV variations of up to  $140 \text{ m s}^{-1}$  with a period of 629 d due to a super-Jupiter companion as well as rotational modulation with a period of 520 d (Hatzes et al. 2015).

Solar-like non-radial oscillations act on much shorter time scales than rotation and were discovered in several of our targets, for example for  $\eta$  Boo (Kjeldsen et al. 2003). Frandsen et al. (2002) detected oscillation periods of as short as 2–5 h in the giant  $\xi$  Hya, another target in this paper. Just recently, Grundahl et al. (2017) identified 49 pulsation modes in the G5 subgiant  $\mu$  Her, originally discovered by Bonanno et al. (2008) as an excess of power at 1.2 mHz. There is also evidence that sub- $\text{m s}^{-1}$  RV oscillations of as short as 50 min were found in HARPS spectra of the active subgiant HR 1362 (Dall et al. 2010) (not part of the target list in this paper). While the solar 5-min oscillation produces only a disk-averaged full RV amplitude of order  $0.5 \text{ m s}^{-1}$  (see paper I, but also Christensen-Dalsgaard & Frandsen 1983; Probst et al. 2015), this amplitude could amount to tens of  $\text{m s}^{-1}$  for K and M giants. For example, Kim et al. (2006) found  $\alpha$  Ari to be a pulsating star with a period of 0.84 d and a RV amplitude of  $20 \text{ m s}^{-1}$  while Hatzes et al. (2012) found for  $\beta$  Gem up to 17 pulsation periods with individual RV amplitudes of up to  $10 \text{ m s}^{-1}$ . A mix of rotational and orbital, and pulsation periods of 230 d and 471 d, respectively, were found for the single-lined M0 giant  $\mu$  UMa (Lee et al. 2016).

In case there are line-profile and RV changes in our targets due to radial or non-radial oscillations, we would then obtain an intrinsically averaged spectrum. For one of the late-type giant targets,  $\beta$  UMi (K4III), Fig. 2 shows a visual comparison of all 22 individual spectra (from 11 consecutive back-to-back exposures in binocular mode) with its combined spectrum. Only a single spectral line is shown; K I 7699 Å ( $\log g_f = -0.176$ ,  $\chi = 1.6 \text{ eV}$ ). Panels a and b are for two levels of magnified details, while the right panel c shows the S/N per pixel just for the line core. Note that the zoom factor in the plot in Fig. 2b is considerable; all there is shown is a  $0.08\text{-}\text{\AA}$  region centered at the K I-7699 line core. The width of the entire plot is approximately one spectral resolution element of UVES or HARPS. We chose this line because of its absorption components from the local interstellar medium (LISM) which, if present, may be used as a reference with respect to the stellar photospheric contribution. No such LISM lines are seen in  $\beta$  UMi. Not unexpected, the largest spread of intensity is found with a 0.3% peak-to-valley (p-v) after 15 min on target (rms of 0.1%), sampled with 11 consecutive 15-s exposures with both LBT telescopes. For

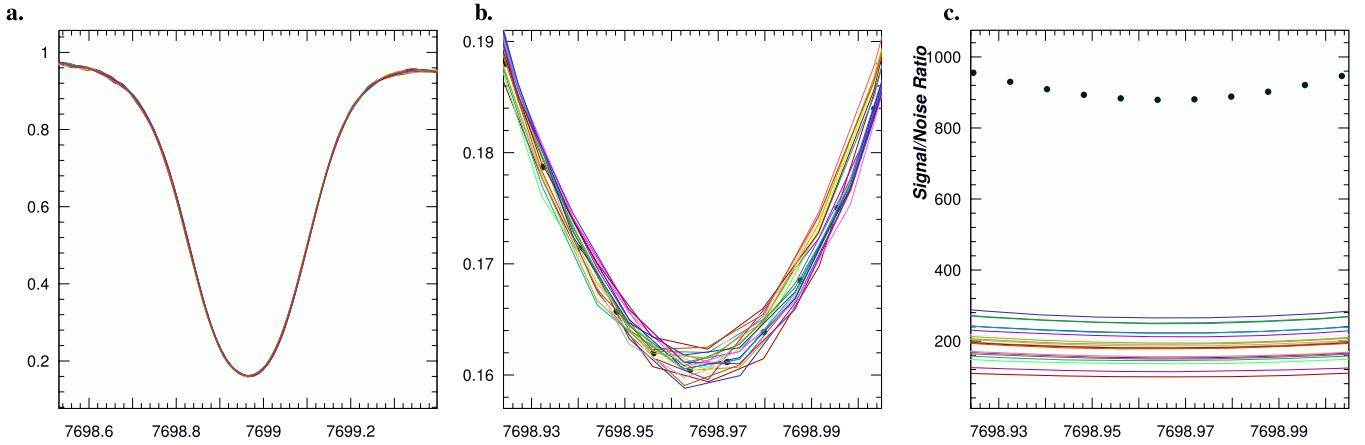


**Fig. 2.** Comparison of an average-combined spectrum and its individual exposures for  $\beta$ UMi (K4III). The  $x$ -axes are wavelengths in  $\text{\AA}$ . The 22 individual exposures are shown as lines, the average combined “deep spectrum” as dots. *Panel a:* a  $0.8\text{-\AA}$  section showing the 22 exposures of the K I  $7699\text{ \AA}$  line profile. The  $y$ -axis is relative intensity. No differences can be seen at this plot scale. *Panel b:* a zoom into a  $0.08\text{-\AA}$  subsection of the line core. The spacing of the dots represent the CCD pixel dispersion. *Panel c:* S/N per pixel in the K I line core for the same spectral window as in *panel b*.

the line core, this spread is expected for the data quality of a single exposure of typical S/N of  $\approx 200$  in the K I-line core. The average-combined spectrum has a S/N of 2250 in the continuum on both sides of the line and still around 900 in the line core itself (Fig. 2c). Therefore, a p-v spread of 0.3% near the continuum is a significant deviation with respect to the photon noise and is likely due to the combined effects of remaining systematic errors (mostly continuum setting) and yet unverified intrinsic stellar variations, presumably non-radial pulsations.

#### 4.3. Signal-to-noise ratio

Table 1 lists the S/N for the deep spectra. S/N is always given for the continuum and per pixel at the mid wavelength of each cross disperser. The variance of each CCD pixel in the raw image is originally calculated after bias subtraction given the measured CCD gain factor for each of the 16 amplifiers of the STA1600LN CCD. The original variance is then propagated at every data reduction step and its final value is used to determine the S/N in every wavelength pixel of the final continuum normalized spectrum. The number of individual spectra employed for a deep-spectrum varies from star to star and is given in the last column of Table 1. It may differ from Table A.1 because not always all existing spectra were included for the combined average spectrum. In case of bad seeing when spectra had significantly lower S/N, or when we had better spectra from different epochs, we simply did not use all of the available spectra but still list them in Table A.1. Several of our dwarf stars (HD 84937, HD 189333, HD 101364, HD 82943, HD 128311, and HD 82106) have S/N below 70:1 at the mid wavelength of CD-I at 400 nm and are thus not recommended for a quantitative analysis at these wavelengths. Note that due to the relatively small fiber entrance aperture of  $0.74''$  the S/N strongly depends on seeing. Blue-arm spectra that were taken only with the VATT and its 450 m fiber generally have lesser S/N. The fibre transmission at 500 nm is 30% (see Strassmeier et al. 2015, their Fig. 41).

Figure 3a is a plot of a typical distribution of S/N across wavelength for one of the targets. Note that wavelength regions at the edges of spectral orders repeat in adjacent orders. Because the order merging procedure in our SDS4PEPSI pipeline is a weighted average of the overlapping wavelength regions, the

S/N for these strips of wavelength is a weighted average from two different orders and thus formally higher than the rest, but not necessarily more accurate due to continuum-setting uncertainties.

#### 4.4. Spectral resolution

As in any échelle spectrograph, the resolution changes along and across each spectral order due to the change of the optical image quality and the anamorphism of the grating. The optical design of PEPSI includes a small  $0.7^\circ$  off-plane angle of the incident beam, which results in a small tilt of  $4^\circ$  of the spectral lines formed by the image slicers. This tilt is compensated by a fixed counter-rotation of the entire image slicer. The residual tilt of the slices that are further away from the optical axis is of the order of  $1^\circ$ , which degrades the resolving power only by  $\approx 2\%$ . The main contributor to the resolving power variations in PEPSI is the change of the optimal focus position across the large area of the two 10 k CCDs.

The nominal spectrograph resolving power vs wavelength was shown in our paper I. The true resolution varied from run to run, in particular for the data taken during commissioning because the line FWHM and, thus, the resolution is computed from the Th-Ar lines at the focus positions achieved at that time. Specifically, we calculated the resolving power for every Th-Ar emission line from its FWHM in pixels and the dispersion at the line position derived from the 3D dispersion polynomial. The best focus position is selected as the maximal median resolving power of all spectral orders vs focus position. An example for July 2016 is shown in Fig. 3b. Focus sequences for every observing run and for all CDs were made with the Th-Ar cathode as the light source. A FFT auto-correlation for a central region on the CCD with  $3000 \times 300$  pixels is applied for focus determination, its FWHM is then converted to effective spectral resolution as a function of wavelength. Our spectra in this paper were all taken with a focus selected to suit all CDs at once. One could do a wavelength dependent focus, that is, refocus for every CD combination, but that was not done for the present data. Therefore, the average resolution for the stars in this paper falls mostly short of  $\lambda/\Delta\lambda$  of 250 000 with a range from 180 000 near the blue cut-off to a peak of 270 000 near 700 nm. The grand average from 383 to 912 nm is approximately 220 000 or  $1.36\text{ km s}^{-1}$ .

**Table 1.** Stellar sample of deep PEPSI spectra.

Star	M-K class	Combined S/N <sup>a</sup>						<i>N</i> spectra <sup>b</sup>
		I/404	II/450	III/508	IV/584	V/685	VI/825	
<i>Giants</i>								
32 Gem	A9 III	100	260	350	470	480	420	222 222
HD 140283	F3 IV	110	210	300	460	480	660	222 224
HD 122563	F8 IV	100	240	400	770	740	750	222 224
$\eta$ Boo	G0 IV	610	980	1400	1700	2180	1660	233 36(10)
$\zeta$ Her	G0 IV	730	240	570	640	1470	2040	286 56(14)
delta CrB	G3.5 III	210	360	500	740	790	1050	122 223
$\mu$ Her	G5 IV	520	870	990	1500	1630	1730	28(13) 8(10)(13)
$\beta$ Boo	G8 III	500	710	1020	1310	1710	1800	3(10)(10) (10)(10)(14)
$\epsilon$ Vir	G8 III	330	130	220	450	730	1970	363 33(11)
$\beta$ Gem	K0 IIIb	400	630	1310	1850	2480	2750	693 83(11)
HD 107328	K0 IIIb	150	430	630	1110	1240	1700	343 436
$\alpha$ UMa	K0 III	330	180	290	640	900	1600	363 339
$\alpha$ Ari	K1 IIIb	680	530	640	1630	1250	1400	366 866
$\alpha$ Boo	K1.5 III	500	1500	1990	3000	5780	4330	6(14)4 7(46)(17)
7 Psc	K2 III	170	470	840	1030	1470	1550	233 334
$\mu$ Leo	K2 III	260	430	750	940	1400	1850	234 34(16)
$\gamma$ Aql	K3 II	180	500	840	1000	1460	1540	2(11)5 56(11)
$\beta$ UMi	K4 III	200	270	510	750	1140	2100	433 33(12)
$\alpha$ Tau	K5 III	550	1280	1920	2680	3100	3480	3(11)8 (12)8(10)
$\mu$ UMa	M0 III	190	240	520	910	1260	2200	396 76(15)
$\gamma$ Sge	M0 III	240	100	380	670	1340	2710	2(13)9 9(10)(17)
$\alpha$ Cet	M1.5 IIIa	300	280	820	1830	1680	1170	326 962
<i>Dwarfs</i>								
$\alpha$ CMa	A1 V	800	590	720	740	620	420	111 111
HD 84937	F2 V	20	110	170	230	250	200	352 523
$\sigma$ Boo	F4 V	490	190	370	420	860	1490	4(10)5 45(18)
HD 49933	F5 V–IV	220	390	670	740	920	620	126 262
$\alpha$ CMi	F5 V–IV	500	410	610	1040	1550	1600	5(12)6 66(14)
$\theta$ UMa	F7 V	550	240	430	660	1110	1670	4(14)8 88(20)
$\beta$ Vir	F9 V	250	90	150	330	440	1220	273 43(10)
HD 22879	F9 V	180	290	260	540	380	780	121 211
HD 189333	F9 V	25	130	225	170	290	270	111 111
HD 159222	G1 V	170	340	450	580	710	800	232 323
16 Cyg A	G1.5 V	100	250	400	530	650	600	122 223
HD 101364	G2 V	40	180	300	350	470	410	336 363
HD 82943	G2 V	35	180	260	340	390	330	322 223
18 Sco	G2 V	240	310	590	1040	1300	850	433 773
51 Peg	G2.5 V	330	710	980	1120	1410	1360	344 445
16 Cyg B	G3 V	180	340	430	700	1110	810	222 263
70 Vir	G4 V–IV	250	450	700	910	1160	1340	222 224
$\mu$ Cas	G5 V	220	400	670	760	980	1000	122 222
HD 103095	G8 V	100	270	450	670	700	740	233 433
$\tau$ Cet	G8.5 V	420	820	1200	1650	1910	1570	566 896
$\epsilon$ Eri	K2 V	410	940	1350	1800	2100	1950	156 565
HD 192263	K2 V	70	200	310	400	590	530	122 222
HD 128311	K3 V	20	120	190	290	350	430	322 223
HD 82106	K3 V	10	75	250	240	480	360	213 132
61 Cyg A	K5 V	105	490	690	990	1350	1080	124 354
61 Cyg B	K7 V	70	200	400	540	850	980	122 224

**Notes.** <sup>(a)</sup> S/N per pixel at the continuum is given for all cross dispersers (CD, roman number) at the respective central wavelengths. For example, for CD I the central wavelength is 404 nm. <sup>(b)</sup> *N* denotes the number of individual exposures per cross disperser, for example “222 222” means two exposures in all six cross dispersers (a parenthesis is used if the number of spectra reached two digits). Note that if the LBT is used, then one exposure means two simultaneous individual spectra (one from each telescope).

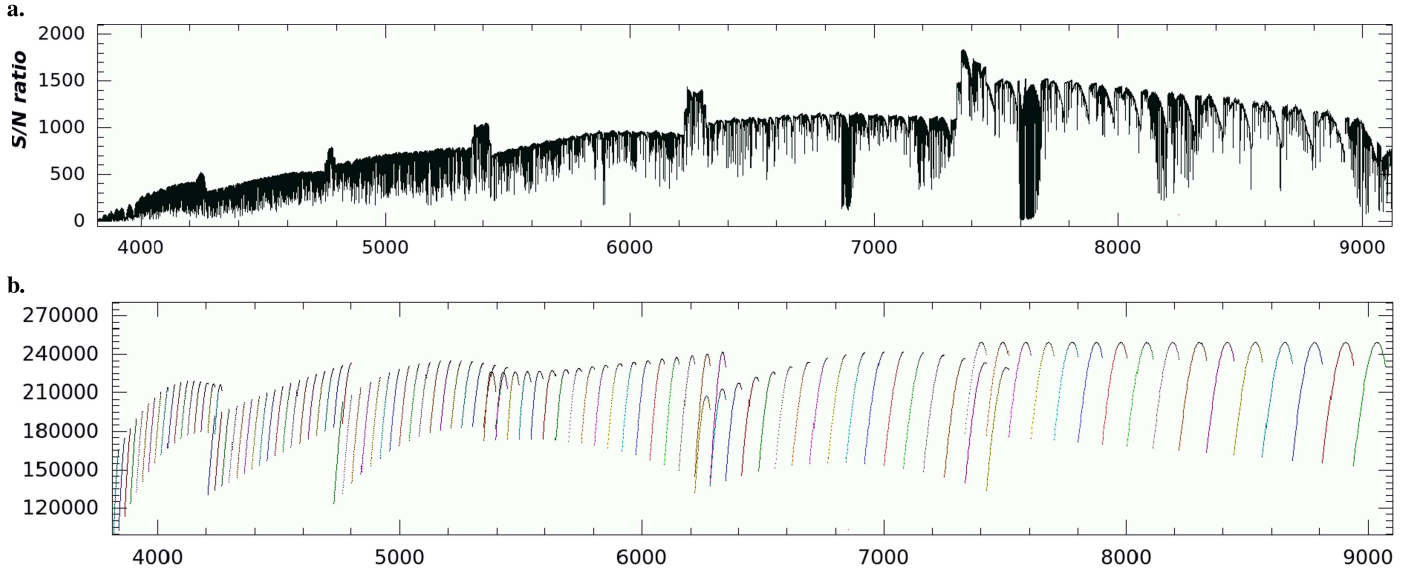


**Fig. 3.** Examples for the typical S/N and spectral resolution of the library stars in this paper. *Panel a:* S/N of the deep spectrum of the G4 subgiant 70 Vir. The larger S/N in the very red wavelengths is mostly due to the larger number of individual spectra. Note that the local peaks in S/N are due to the wavelength overlap of the cross dispersers, which effectively doubles the number of pixels there. *Panel b:* spectral resolution for the focus achieved for the July 2016 run.

When modeling individual spectral regions, or line profiles, it is advisable to consult Fig. 3b or the FITS header for the true resolution at a particular wavelength. Resolution dispersion is approximately  $\pm 30\,000$  for the entire 383 to 912 nm range.

#### 4.5. Continuum

Continuum-setting errors are among the largest uncertainties for high-resolution spectroscopy. It is particularly problematic for cool stars where line blanketing effectively removes any clean continuum signature. This is typical for blue wavelengths short of  $\approx 450$  nm as well as those red wavelengths that are affected by the wide terrestrial  $O_2$  absorption bands. It is generally the case for M stars due to increasing molecular bands with decreasing effective temperature. For solar-like stars in this paper, we referenced to the dry NSO FTS solar spectrum for continuum definition just like we did in paper I for the Sun itself. For  $\approx K1$  giants, we use as a reference the KPNO Arcturus atlas from Hinkle et al. (2000). The final continuum is obtained from synthetic spectra. We tabulated synthetic spectra generated with the MARCS model atmospheres (Gustafsson 2007), the VALD atomic line list (Kupka et al. 2011), the SPECTRUM code (Gray & Corbally 1994), and the atmospheric parameters from the literature (taken from Blanco-Cuaresma et al. 2014). These synthetic spectra are first trimmed to the reference stars (Sun and Arcturus) and then employed to build a continuum free of spectral lines, which is then used for division for all targets of the atlas. We noticed a systematic opacity deficiency for giant-star spectra near our blue cut-off wavelength. Currently, we bypassed this by fitting the Arcturus atlas and deriving a fudge parameter that is then multiplied with the synthetic continuum.

There will always be residual continuum errors left in the data. For the red spectra these are generally caused by the increasing telluric contamination toward longer wavelengths. Although a small effect, it can cause systematic shifts at some wavelength regions of the order of 1%. However, such small shifts may simply be compensated posteriori to the data reduction. More problematic is the line blanketing in the blue

together with the lowered S/N of the blue spectra in general. It can lead to continuum errors of 10–20% for the regions bluer than 397 nm. Targets with very low S/N near the blue cut-off wavelength may appear with line depths that are negative and peaks that are above continuum. When comparing these PEPSI spectra to synthetic spectra it is advisable to also refit the continuum level in question.

#### 4.6. RV zero point

In paper I, we have shown that our absolute RV zero point was within a rms of just  $10\text{ m s}^{-1}$  of the HARPS laser-comb calibrated solar atlas (Molaro et al. 2013). This allows us to combine spectra taken over a long period of time, at least as long as the spectrograph chamber is not opened. Besides, there is a small systematic difference of on average  $9\text{ m s}^{-1}$  between the zero points of LBT SX and LBT DX spectra due to its separate light coupling. The shift between SX and DX is not a single constant but depends on the CD, ranging between 5 to  $30\text{ m s}^{-1}$ . The major contribution is because SX and DX have different foci, hence the stellar images can be offset from one another. We will investigate further whether the shift can be compensated with the simultaneous FPE reference source. For the present paper, any differential RV shifts were removed for each individual CD by means of a least-squares minimization with respect to the SX side. Larger than expected shifts occurred during commissioning because we realigned the CDs once in the blue arm and twice in the red arm, and the spectrum image had unavoidably moved on the detector. Despite that these data periods were treated with special attention, it created residual RV inhomogeneities of the order of the uncertainties themselves. Because we do not intend to provide RVs for the library stars, we shifted all spectra in this library to their respective barycentric RV value by subtracting the RV given in the header of the respective FITS file. This shall enable easier inter comparisons. The date given in the average combined FITS file is the average date resulting from the combination of the individual CDs, it has no physical meaning.

**Table 2.** Wavelength regions in Å that are affected by a bad-amplifier problem with the Blue CCD for the epoch November–December 2015.

# <sup>a</sup>	CD-III	#	CD-II	#	CD-I
120	5063–5103	136	4484–4501	151	4025–4056
119	5106–5145	135	4501–4534	150	4052–4083
118	5150–5161	134	4534–4570	149	4080–4096

**Notes.** <sup>(a)</sup> Échelle order. Stars (CDs) affected are 51 Peg (I,II), 7 Psc (I,II,III),  $\alpha$  Ari (II,III), and  $\alpha$  Cet (II,III).

#### 4.7. Wavelength coverage

The free spectral range for each CD has been graphically shown in our technical paper in [Strassmeier et al. \(2015\)](#) as well as in paper I, and we refer the reader to these papers for more details. Here we recap the wavelength coverage in nm for each cross disperser; CD-I 383.7–426.5, CD-II 426.5–480.0, CD-III 480.0–544.1, CD-IV 544.1–627.8, CD-V 627.8–741.9, and CD-VI 741.9–912. All spectra in this paper cover the full wavelength range 383–912 nm. Because of the comparably low efficiency in the bluest cross disperser (CD-I), and the accordingly longer exposure times, its exposures had sometimes to be done on different nights for some targets. For a total of six dwarf-star targets, we lacked the telescope time to redo the CD-I exposure with an appropriate longer integration time (see Sect. 4.3). Their initial spectra provided only poor S/N for wavelengths shorter than or around Ca II H&K, and we recommend not to use these wavelength sections for the six stars. For one of these target, HD 82106, we did not include the spectrum shorter than 398 nm because it affected the continuum setting for the remaining wavelengths of CD-I. For the other five stars, we decided to keep these wavelengths in the library for the sake of completeness. Note that the bluest wavelength regions are not accessible with the VATT because of the 450-m fibre link and its effectively 95% absorption loss at 400 nm. The stars affected can also be identified in Table A.1 by their two-digit S/N for CD I/404 nm.

#### 4.8. Blemishes

Four stars observed in the time frame November–December 2015 have only a fractal wavelength coverage in the blue arm. On Nov. 13, 2015, we discovered a degrading amplifier in the blue 10k CCD that left its section on the CCD (approximately  $5000 \times 1280$  pixels) with an effective gain of 1.2 instead of 0.5. This in turn resulted in a non-linear behavior at our exposure levels and lowered the quantum efficiency, which both caused intensity jumps in the spectrum at the amplifier edges and thus confused the order tracing algorithm of the data reduction. It affects one half of altogether three échelle orders. The jumps were corrected and spectra extracted but with approximately half the S/N for the regions affected. The chip was repaired in early 2016 and the problem did not occur again (bonding at the CCD had gotten loose and introduced a variable ohmic resistance). The consequence of this is that we do not recommend to use the wavelength regions of this section of the blue CCD of the four stars (51 Peg, 7 Psc,  $\alpha$  Ari, and  $\alpha$  Cet), which were all taken during above time window. Table 2 lists the detailed wavelengths affected.

Several of the spectra show a (time-variable) HeNe-laser emission line at 6329 Å. This line was picked-up accidentally as stray light from the LBT laser tracker system (which should have been turned off). Its FWHM is around 53 mÅ and its shape

appears rather asymmetric with an emission intensity of up to 1.4 relative to the (stellar) continuum. Spectra are usually not affected unless the laser line falls within a stellar line like, for example in the 61 Cyg A spectra taken during the May 2015 run.

#### 4.9. A comparison with the KPNO Arcturus atlas

[Hinkle et al. \(2000\)](#) assembled an atlas spectrum of Arcturus from a large number of individual spectral segments obtained with the KPNO coude feed telescope and spectrograph at Kitt Peak. It took 15 nights to complete all exposures (from Apr. 20 to June 13, 1999). Its spectral resolution ranges between 130 000 to 200 000 for the wavelength range 373 to 930 nm and has been an outstanding reference for more than a decade. It succeeded the photographic Arcturus atlas of [Griffin \(1968\)](#).

We employ the KPNO atlas spectrum to find its continuum and use it for PEPSI division. Then, the PEPSI spectrum matches the KPNO spectrum almost perfectly. Figure 4a shows a comparison of the KPNO atlas and the PEPSI spectrum for the Fraunhofer G-band. PEPSI's slightly higher spectral resolution shows up with slightly deeper lines, on average 0.5% deeper than the KPNO lines (in particular in the red wavelengths). The wavelength distribution of the achieved S/N is rather inhomogeneous for the PEPSI spectrum because CD-III was employed for only four short VATT exposures while CD-VI had included nine LBT exposures (exposure time with the LBT was 3 s, with the VATT 4 min for similar S/N). Redward of  $\approx 400$  nm the photon noise is not noticeable anymore in the plots, peaking at 6000:1 at 710 nm, but is inferior than the KPNO atlas for the very blue parts shorter than  $\approx 397$  nm, where values below 100:1 are reached.

The wavelength zero point of the KPNO and the PEPSI spectra differs by several hundred m s<sup>-1</sup>. A cross correlation of each PEPSI spectrum with the appropriate part of the KPNO atlas suggests the following shifts PEPSI-minus-KPNO in m s<sup>-1</sup> (CD-I 545, CD-II 631, CD-III 576, CD-IV 740, CD-V 783, and CD-VI 871). Note that the higher differences for the red CDs are due to the increase of telluric lines in these wavelength regions which makes the cross correlation more prone to systematic errors. When comparing the two spectra these shifts were applied so that both spectra are in barycentric rest frame. The pixel-to-pixel ratio spectrum (PEPSI spectrum divided by the KPNO atlas) is in general dominated by the variable water content of Earth's atmosphere which creates numerous artifacts. Three wavelength sections containing the Ca II H line core, H $\alpha$ , and Li I 6708 are shown in Fig. 4b. The presence of emission in the cores of these lines is a simple diagnostic of magnetic activity in the chromospheres of late-type stars. As can be seen in Fig. 4b, the ratio spectrum shows weak differences in the Ca II H and H $\alpha$  profiles at a few per cent level (10% peak-to-valley in the H&K line core and 8% in H $\alpha$ ). Note that the time difference between the KPNO spectrum and the PEPSI spectrum is 16 years. We usually interpret such residual emission due to changing magnetic activity. While just a preliminary result, it supports the earlier claims of the existence of both Ca II H&K variability (with a period of  $\leq 14$  yr) by [Brown et al. \(2008\)](#) and the detection of a (very weak) longitudinal magnetic field by [Hubrig et al. \(1994\)](#) and [Sennhauser & Berdyugina \(2011\)](#).

## 5. Notes on the stellar sample

The sample in Table 1 consists mostly of the *Gaia* FGK benchmark stars ([Blanco-Cuaresma et al. 2014](#)) that are accessible from the northern hemisphere. These are complemented by a few

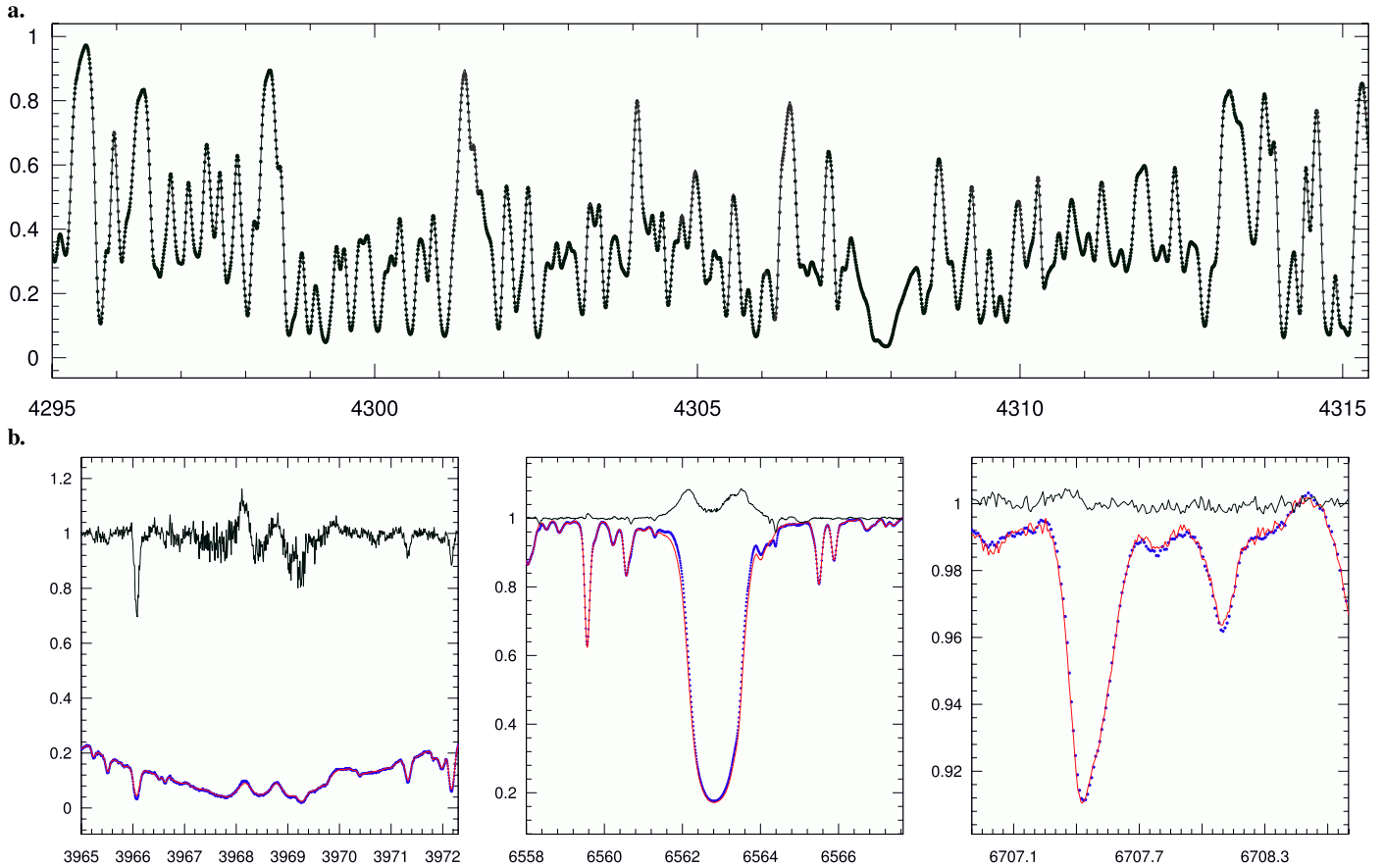


**Fig. 4.** Comparison of the deep PEPSI spectrum of Arcturus with the KPNO Arcturus atlas from [Hinkle et al. \(2000\)](#). *Panel a*: numerous CH lines centered around the Fe I/Ca I blend at 4308 Å that constitute the Fraunhofer *G*-band. The dots are the PEPSI spectrum and the line is the KPNO atlas. The match is nearly perfect. *Panel b*: three wavelength regions where chromospheric activity may be detected. Each panel shows the ratio spectrum PEPSI:KPNO (line around unity), the KPNO spectrum as a line, and the PEPSI spectrum as dots. From *left to right*, the core of the Ca II H line, H $\alpha$ , and the Li I 6707.9-Å line region.

well-known Morgan-Keenan spectroscopic standard stars from the list of [Keenan & McNeil \(1989\)](#) and partly available in the PASTEL database ([Soubiran et al. 2010](#)). A few stars were added that we had kept as serendipitous references from the STELLA binary survey ([Strassmeier et al. 2012](#)).

### 5.1. Giants

Chemical abundances and evolutionary indicators of giants are widely used as probes for the galactic chemical evolution but their precision and accuracy continue to remain a challenge ([Gustafsson 2007](#); [Luck & Heiter 2007](#); [Luck 2014](#)). We provide spectra for 22 red giant branch (RGB) stars and subgiants in the present library. These are mostly very bright and well-studied stars like Arcturus ( $\alpha$  Boo) or Procyon ( $\alpha$  CMi) but include a few less well-studied targets like 32 Gem (=HD 48843, HR 2489) or 16 Vir (=HD 107328). Spectral M-K classifications are rather mature for these bright targets except maybe for 32 Gem which had been listed as A9 III by [Morgan \(1972\)](#), A7 II by [Cowley & Crawford \(1971\)](#), A9 II-III by [Cowley & Fraquelli \(1974\)](#), and most recently, as A8 II by [Fekel \(2003\)](#). Given the deep and structured Na D and K I absorption profiles it must be distant and thus likely a bright-giant star. Another target,  $\gamma$  Aql (HD 186791), has been consistently identified in the literature as a K3 bright giant of luminosity class II since the fifties of the last century ([Morgan & Roman 1950](#)), although [Keenan & Hynek \(1945\)](#) assigned a K3 supergiant classification

based on infrared spectra. Three M giants comprise the very cool end of our classification sequence; two M0 III stars ( $\mu$  UMa = HD 89758 and  $\gamma$  Sge = HD 189319) and one M1.5 III ( $\alpha$  Cet = HD 18884). Just recently, [Lee et al. \(2016\)](#) reported secondary RV variations of the (single-lined) spectroscopic binary  $\mu$  UMa and concluded on an origin from pulsations and chromospheric activity. Planetary companions were found for the two K giants  $\mu$  Leo and  $\beta$  UMi ([Lee et al. 2014](#)). [Lebzelter et al. \(2012\)](#) presented a comparative spectroscopic analysis of two cool giants that are also in the present paper;  $\alpha$  Tau (K5 III) and  $\alpha$  Cet.

### 5.2. Dwarfs

Spectra for 26 dwarfs are presented. Note that the benchmark star HD 52265 (G0V) was observed only during a bad weather epoch with the VATT and therefore we do not include it into the PEPSI library but still keep its entry in the observing log in [Table A.1](#). During a search for the white dwarf companion of  $\alpha$  Cma (Sirius), we took a spectrum of its A1 V primary, the brightest star in the sky, which we include in this paper for the sake of spectral mining. HD 189333 = BD+38 3839 ( $V = 8^m.5$ ), a star similar and close to the famous planet-transit star HD 189733, was classified F5 V from photographic spectra by as long ago as [Nassau & MacRae \(1949\)](#), which is pretty much all there is known for this star. We took a single spectrum of it and make it available in the library. Another target, HD 192263, has a checkered history as a planet host, see the full story in the introduction in the paper by

Dragomir et al. (2012). Its planet was found, lost, and re-found in the course of a couple years. Our spectrum shows the star with strong Ca II H&K emission and thus being chromospherically very active. Another planet-host star recently revisited in the literature (McArthur et al. 2014 and references therein) is HD 128311 =  $\nu$  And. Together with  $\epsilon$  Eri it is among the targets known to contain planets and debris disks.

## 6. Representative science examples

### 6.1. Global stellar parameters

Global stellar surface parameters like effective temperature, gravity, and metallicity are basics for our understanding of stars. Observed spectra are usually compared to synthetic spectra from model atmospheres, analog to what had been exercised for the benchmark stars of the *Gaia*-ESO survey and many other such attempts in the literature (e.g., Paletou et al. 2015). The main advantage to do so again for benchmark stars is the homogeneity of the data in this paper and their significantly higher spectral resolution. There is no need to homogenize the data by artificially broadening the spectra to match the resolution of the lowest contributor. For a first trial, we employ our spectrum synthesis code ParSES to two selected deep spectra; 70 Vir (G4V-IV) and  $\alpha$  Tau (K5III). ParSES is based on the synthetic spectrum fitting procedure of Allende-Prieto et al. (2006) and described in detail in Allende-Prieto (2004) and Jovanovic et al. (2013).

Model atmospheres were taken from MARCS (Gustafsson 2007). Synthetic spectra are pre-tabulated with metallicities between  $-2.5$  dex and  $+0.5$  dex in steps of 0.5 dex, logarithmic gravities between 1.5 and 5 in steps of 0.5, and temperatures between 3500 K and 7250 K in steps of 250 K for a wavelength range of 380–920 nm. This grid is then used to compare with selected wavelength regions. For this paper, we used the wavelength range of only one of the six cross dispersers (CDIV 544.1–627.8 nm). We adopted the *Gaia*-ESO clean line list (Jofré et al. 2014) with various mask widths around the line cores between  $\pm 0.05$  to  $\pm 0.25$  Å. Table 3 summarizes the best-fit results. We emphasize that these values are preliminary and meant for demonstration.

We first applied ParSES to the PEPSI solar spectrum, same wavelength range and line list as for the other two example stars. It reproduces the expected basic solar parameters very well (Table 3). Its parametric errors based on the  $\chi^2$  fit are likely not representative for the other stars because we adopted the NSO FTS continuum for rectification.

70 Vir is more a subgiant than a dwarf. A  $\log g$  of 3.89 was given by Fuhrmann et al. (2011) based on the HIPPARCOS distance from which the iron ionization equilibrium temperature of 5531 K results. A previous FOCES analysis by (Bernkopf et al. 2001) gave  $5481 \pm 70$  K,  $\log g$  of  $3.83 \pm 0.10$ , and a metallicity of  $-0.11 \pm 0.07$ , the latter was revised to  $-0.09 \pm 0.07$  from a single BESO spectrum (Fuhrmann et al. 2011). Its  $v \sin i$  of 1.0 was just mentioned in a figure caption and it is not clear whether this was actually derived or assumed. Jofré et al. (2014) lists results from an ELODIE spectrum with 5559 K and a  $\log g$  of 4.05. Our values are 5475 K,  $\log g$  of 3.86, and with a metallicity of  $-0.13$ . A rotational broadening was actually not detected.

$\alpha$  Tau's stellar parameters were determined by many sources summarized in Heiter et al. (2015). Its  $T_{\text{eff}}$  ranges between 3987 and 3887 K, its  $\log g$  between 1.20 and 1.42. Our values are 3900 K,  $\log g$  of 1.45, and a metallicity of  $-0.33$ . Continuum setting for  $\alpha$  Tau was iteratively improved but many unknown lines

**Table 3.** Example results from PEPSI using ParSES.

	$T_{\text{eff}}$ (K)	$\log g$ (cgs)	[Fe/H] (solar)	$\xi_t$ (km s $^{-1}$ )	$v \sin i$ (km s $^{-1}$ )
Sun					
PEPSI	5730 $\pm 50$	4.44 $\pm 0.15$	$-0.04$ $\pm 0.15$	1.2 $\pm 0.2$	0.0 $\pm 1$
70 Vir					
PEPSI	5475 $\pm 50$	3.86 $\pm 0.15$	$-0.13$ $\pm 0.1$	1.29 $\pm 0.1$	0.0 $\pm 1$
FOCES	5481 $\pm 70$	3.83 $\pm 0.10$	$-0.11$ $\pm 0.07$	...	1.0 $\pm$
ELODIE	5559 $\pm 19$	4.05 $\pm 0.04$	$-0.06$ $\pm 0.02$	1.11 $\pm 0.06$	1.36 $\pm 0.45$
$\alpha$ Tau					
PEPSI	3900 $\pm 50$	1.45 $\pm 0.3$	$-0.33$ $\pm 0.1$	1.16 $\pm 0.1$	3.5 $\pm 1.5$
Benchmark	3927 $\pm 40$	1.11 $\pm 0.15$	$-0.37$ $\pm 0.17$	1.63 $\pm 0.30$	5.0 ...

**Notes.**  $\xi_t$  is the microturbulence; FOCES refers to Fuhrmann et al. (2011). ELODIE refers to Jofré et al. (2014). Benchmark refers to Heiter et al. (2015) for  $T_{\text{eff}}$  and  $\log g$ , and to Jofré et al. (2014) for metallicity.

make the fit vulnerable to line-list deficiencies. Also note that the  $v \sin i$  of 3.5 km s $^{-1}$  from our  $R = 220\,000$  spectra is smaller than any other value published so far. Otherwise, the benchmark values are matched properly.

### 6.2. Rare-earth elements

Figure 5 shows the detection of the rare-earth element dysprosium ( $Z = 66$ ). The figure plots several stars ranging from main-sequence stars like the Sun and 70 Vir to the RGB stars  $\alpha$  Boo,  $\alpha$  Ari, and  $\mu$  Leo (all  $\approx$ K1-2 III). The singly-ionized Dy line at 4050.55 Å is indicated with a vertical line. Dysprosium's name comes from greek dusprositos and means "hard to get at", which spurred us to use it as a case example. The Dy II line shown is weak and almost buried by a nearby Zr II, an Fe I, and an unidentified line blend, but still among the more easily detectable lines. There are many more Dy lines in the spectral range of PEPSI that could be exploited for an abundance determination. The element has been detected in the solar spectrum as well as in some Ap stars (e.g., Ryabchikova et al. 2006) and is possibly synthesized only in supernovae. Experimental wavelengths and oscillator strengths for Dy II lines are available from Wickliffe et al. (2000).

### 6.3. Carbon $^{12}\text{C}$ to $^{13}\text{C}$ ratio

Meléndez et al. (2009) have shown that the Sun exhibits a depletion of refractory elements relative to volatile elements and related this to a cleansing effect during its rocky-planet formation. The engulfment of a close-orbiting planet during the RGB evolution may lead to the opposite effect, an overabundance of refractory elements, if fully transferred to the envelope of the host star. Various authors searched for signatures of such a replenishment in the Li abundances and its isotope ratio (e.g., Kumar et al. 2011) but also in  $^{12}\text{C}/^{13}\text{C}$  (e.g., Carlberg et al. 2012). Accurate C-isotope ratios require high-resolution and high S/N spectra while applicable only to stars cool enough to

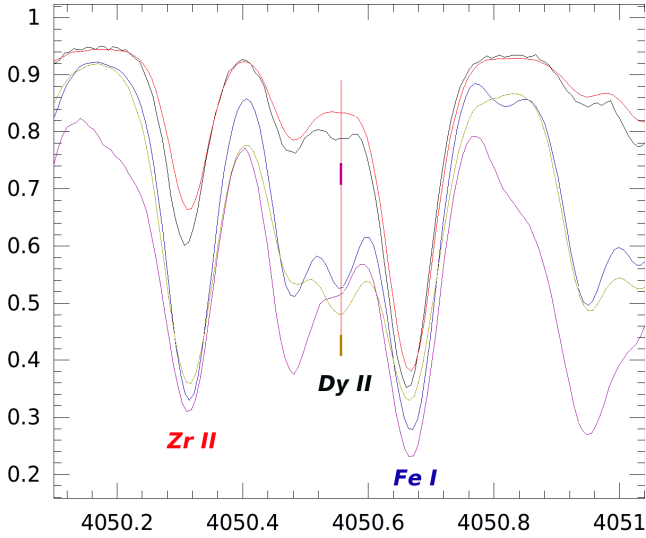


**Fig. 5.** Detection of the rare-earth element dysprosium (Dy) in the spectra of several library stars (from *top to bottom* for the Fe I line core; Sun, 70 Vir,  $\alpha$  Boo,  $\alpha$  Ari,  $\mu$  Leo). Dysprosium’s name comes from greek dusprositos and means “hard to get at”. The singly-ionized Dy line at 4050.55 Å is indicated along with one Zr II and one Fe I line.

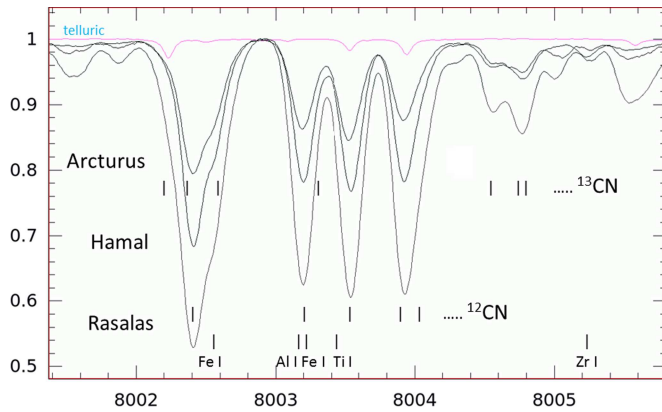


**Fig. 6.** Comparison of the 800-nm region of three RGB stars in this library; from *top to bottom*, Arcturus ( $\alpha$  Boo, K1.5III), Hamal ( $\alpha$  Ari, K1IIIb), Rasalas ( $\mu$  Leo, K2III). The region contains many  $^{12}\text{C}$ N and  $^{13}\text{C}$ N lines from which the  $^{12}\text{C}$  to  $^{13}\text{C}$  ratio is derived. A telluric spectrum scaled to the Rasalas observation is shown on the *top*.

enable CN formation and with low  $v \sin i$  (e.g., Berdyugina & Savanov 1994). No conclusive statements on engulfing could be made so far from carbon abundances but it seems clear that initial protostellar Li abundances and  $^{12}\text{C}/^{13}\text{C}$  may be more diverse than originally thought (Carlberg et al. 2012). It is thus advisable also analyzing the carbon isotope ratio in benchmark RGB stars.

Figure 6 shows a comparison of the 800-nm region of three of the RGB stars in this paper (Arcturus, K1.5III; Hamal, K1IIIb; and Rasalas, K2III). The measurement of  $^{12}\text{C}/^{13}\text{C}$  usually comes from fitting a small group of CN lines in the spectral region between 8001 and 8005 Å. There, one can see the isotope ratio even by eye, that is, by comparing the 8004 Å line depth, which is solely due to  $^{12}\text{C}$ N, to the depth of the feature at 8004.7 Å, which is solely due to  $^{13}\text{C}$ N. CN identifications in the plot were taken from Carlberg et al. (2012). Spectra of this region are contaminated by telluric lines. We have demonstrated this in

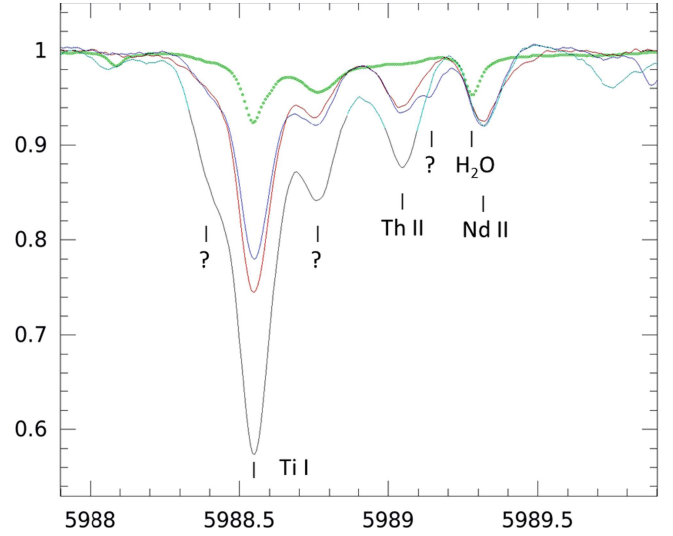


**Fig. 7.** Th II 5989.045-Å and Nd II 5989.378-Å lines in three RGB stars (full lines, from *top to bottom* in the Ti I line core; Arcturus, Hamal, Rasalas). The *top* spectrum shown as dots is a spectrum of the Sun.

paper I for the solar spectra and for the solar twin 18 Sco. Figure 6 shows for comparison the Kurucz et al. (1984) telluric spectrum. For our plot the telluric spectrum was scaled and shifted to match the observed telluric spectrum of  $\mu$  Leo (and can thus only be compared to the  $\mu$  Leo spectrum in the plot in Fig. 6). It is self explaining that one should take its contamination into account when determining the carbon isotope ratio.

#### 6.4. Heavy elements

The formation of very heavy elements like uranium ( $Z=92$ ) or thorium ( $Z=90$ ) requires a process with rapid neutron capture, the so-called r-process, which is naturally happening during supernova explosions. The explosion ejects these elements into space where they are then available for the next generation of stars. Common uranium isotopes have half-life decay times of  $10^8$  to  $10^9$  years, and had been used to determine the age of the universe by observing ultra-metal-poor stars (Frebel et al. 2007). Gopka et al. (2007) identified Th II 5989.045 Å in the KPNO Arcturus spectrum from Hinkle et al. (2000). They followed this up by the identification of more such lines from the KPNO atlas (Gopka et al. 2013). The most widely used line is Th II 4019.129 Å. Together with the nearby neodymium line Nd II 4018.8 Å this line is used to form the chronometric ratio Th/Nd, first suggested by Butcher (1987) as an age indicator. However, there is no systematic identification of heavy-element lines in benchmark stars.

We have visually searched our library sample for the strong lines of U II at, for example 3859.57 Å and 4241.67 Å as well as Th II at 4019.129 Å and 5989.045 Å, leaning on new oscillator strengths from Nilsson et al. (2002a,b). Some of these lines are indeed identified, for example the Th II-Nd II line pair at 5989 Å in giant stars like Arcturus,  $\alpha$  Ari, or  $\mu$  Leo or the U II transition at 4241-Å in  $\epsilon$  Vir. Figure 7 is a comparison of above three targets with the Sun for the Th 5989-Å region. For many others there is only vague evidence due to blending. Note again that the solar spectrum in this plot was also taken with PEPSI in the same manner as the other stars. It shows a dominant telluric blend on the blue side of the expected Nd II line. Th II 5989.045

may be present in the solar spectrum with an upper limit at the  $<1 \text{ m}\text{\AA}$  level.

In connection with chronometry, the s-process elements Ba and Sr (a.o.) are also key elements. The most prominent barium line is the one Ba II transition at  $4554.02 \text{ \AA}$ . Other comparably weaker lines are  $3891.78 \text{ \AA}$  and  $4130.64 \text{ \AA}$  (see, e.g., Siqueira Mello et al. 2014). Strontium lines are comparably more prominent than U and Th, for example Sr II at  $4077.72 \text{ \AA}$  or  $5215.52 \text{ \AA}$ . The  $4077\text{-}\text{\AA}$  line is commonly used in the M-K system to classify cool, low-gravity, stellar atmospheres because of its density sensitivity (Gray & Garrison 1989). Our library spectra may be used to investigate spectral lines from heavy elements in greater detail than before.

## 7. Summary

We present a library of high-resolution (on average  $\approx 220\,000$ ), high-S/N optical spectra of a sample of 48 bright reference stars. The sample includes the northern *Gaia* benchmark stars and a few well-known M-K standards. Deep spectra are built by average combining individual exposures and reach S/N of many hundreds and, in some cases, even thousands. Continua are set by predetermining synthetic spectra that match the target classification. Continuum adjustments of several tens of per cent were necessary for wavelengths shorter than 400 nm. For all other wavelengths the differences in the continuum were always less than 1% and for wavelength regions with clear continuum visibility more like 0.2%.

A comparison with the KPNO Arcturus atlas revealed nearly perfect agreement with our library spectrum. At some wavelength regions the pixel-to-pixel differences are equal to or comparable to the photon noise level after both spectra were shifted in wavelength to the barycentric rest frame. We also found very weak Ca II H&K and H $\alpha$  residual emission in Arcturus, thereby further strengthening earlier claims that it has a magnetic field and even an H&K activity cycle. The spectrum is still to be examined in detail whether the match also holds for other spectral lines. After all, the two spectra were taken 16 yr apart.

We identified several archival science cases possible to be followed up with the present data. Among these are the determination of global stellar parameters like effective temperature, gravity, metallicity, and elemental abundances. For a demonstration, we applied our spectrum synthesis code ParSES to a number of selected wavelength regions of 70 Vir (G4V-IV) and  $\alpha$  Tau (K5III). The resulting values are summarized and compared with the literature in Table 3. These numbers are not intended to be the final verdict but shall just demonstrate the capabilities and the expected uncertainties.

Of particular interest are isotopic line ratios. The most asked for in the literature is the  ${}^6\text{Li}$  to  ${}^7\text{Li}$  ratio from the two Li doublets at  $6708 \text{ \AA}$ . Its science cases range from rocky planet engulfment, internal stellar mixing and dredge-up mechanisms, to the primordial Li production rate. In our paper I on the Sun-as-a-star, we had analyzed this wavelength region of the Sun in detail and refer the reader to this paper. Another isotope ratio of general interest is  ${}^{12}\text{C}/{}^{13}\text{C}$ . Its primary science case is the main chain of the CNO cycle in stellar evolution but also allows the quantification of dredge-up episodes on the RGB in more detail. Finally, elemental abundances of species “that are hard to get at” are made accessible, for example the rare-earth element dysprosium or the heavy elements uranium and thorium, just to name a few.

The reduced deep spectra can be downloaded in FITS format from our web page<sup>2</sup>. We also provide the deep 1D data prior to the final continuum normalization.

*Acknowledgements.* We thank all engineers and technicians involved in PEPsi, in particular our Forschungstechnik team and its late Emil Popow who passed away much too early, but also Mark Wagner and John Little and his LBTO mountain crew. Our thanks also go to Christian Veillet, LBT director, and to Paul Gabor, VATT director, for their clever telescope scheduling. Walter Seifert, LSW Heidelberg, is warmly thanked for making some hours of his LUCI commissioning time available to us. It is also our pleasure to thank the German Federal Ministry (BMBF) for the year-long support through their Verbundforschung for LBT/PEPSI through grants 05AL2BA1/3 and 05A08BAC. Finally, the many telescope operators are thanked for their patience and even –partial– enthusiasm when we wanted to observe Sirius with a 12 m telescope. This research has made use of the SIMBAD database, operated at CDS, Strasbourg, France.

## References

- Allende-Prieto, C. 2004, *Astron. Nachr.*, **325**, 604  
 Allende-Prieto, C., Beers, T. C., Wilhelm, R., et al. 2006, *ApJ*, **636**, 804  
 Aurière, M. 2003, eds. J. Arnaud & N. Meunier, in *EAS Pub. Ser.* **9**, 105  
 Bagnulo, S., Jehin, E., Ledoux, C., et al. 2003, *The Messenger*, **114**, 10  
 Berdyugina, S. V., & Savanov, I. S. 1994, *Astron. Lett.*, **20**, 639  
 Bernkopf J., Fiedler A., & Fuhrmann K. 2001, in *Astrophysical Ages and Times Scales*, eds. T. von Hippel, C. Simpson, & N. Manset (San Francisco: ASP), *ASP Conf. Ser.*, **245**, 207  
 Blanco-Cuaresma, S., Soubiran, C., Jofre, P., & Heiter, U. 2014, *A&A*, **566**, A98  
 Bonanno, A., Benatti, S., Claudi, R., et al. 2008, *ApJ*, **676**, 1248  
 Brown, S. F., Gray, D. F., & Baliunas, S. L. 2008, *ApJ*, **679**, 1531  
 Butcher, H. 1987, *Nature*, **328**, 127  
 Carlberg, J. K., Cunha, K., Smith, V. V., & Majewski, S. R. 2012, *ApJ*, **757**, 109  
 Christensen-Dalsgaard, J., & Frandsen, S. 1983, *Sol. Phys.*, **82**, 469  
 Cowley, A., & Fraquelli, D. 1974, *PASP*, **86**, 70  
 Cowley, A. P., & Crawford, D. L. 1971, *PASP*, **83**, 296  
 Creevey, O. L., Thévenin, F., Berio, P., et al. 2015, *A&A*, **575**, A26  
 Dall, T. H., Bruntt, H., Stello, D., & Strassmeier, K. G. 2010, *A&A*, **514**, A25  
 Dekker, H., D’Odorico, S., Kaufer, A., Delabre, B., & Kotzlowski, H. 2000, *SPIE*, **4008**, 534  
 Dragomir, D., Kane, S. R., Henry, G. W., et al. 2012, *ApJ*, **754**, 37  
 Fekel, F. C. 2003, *PASP*, **115**, 807  
 Frandsen, S., Carrier, F., Aerts, C., et al. 2002, *A&A*, **394**, L5  
 Frebel, A., Christlieb, N., Norris, J. E., et al. 2007, *ApJ*, **660**, L117  
 Fuhrmann, K., Chini, R., Hoffmeister, V. H., et al. 2011, *MNRAS*, **411**, 2311  
 Gilmore, G., Randich, S., Asplund, M., et al. 2012, *The Messenger*, **147**, 25  
 Gopka, V. F., Vasileva, S. V., Yushchenko, A. V., & Andrievsky, S. M. 2007, *Odessa Astron. Publ.*, **20**, 58  
 Gopka, V. F., Shavrina, A. V., Yushchenko, V. A., et al. 2013, *Bull. of the Crimean Astrophys. Obs.*, **109**, 41  
 Gray, R. O., & Corbally, C. J. 1994, *AJ*, **107**, 742  
 Gray, R. O., & Garrison, R. F. 1989, *ApJS*, **69**, 301  
 Griffin, R. F. 1968, A photometric atlas of the spectrum of Arcturus,  $\lambda 3600\text{--}8825\text{\AA}$  (Cambridge: Cambridge Philosophical Society)  
 Grundahl, F., Fredslund Andersen, M., Christensen-Dalsgaard, J., et al. 2017, *ApJ*, **836**, 142  
 Gustafsson, B. 2007, in *Why Galaxies Care About AGB Stars: Their Importance as Actors and Probes*, eds. F. Kerschbaum, C. Charbonnel, & R. F. Wing (San Francisco: ASP), *ASP Conf. Ser.*, **378**, 60  
 Hatzes, A. P., Zechmeister, M., Matthews, J., et al. 2012, *A&A*, **543**, A98  
 Hatzes, A. P., Cochran, W. D., Endl, M., et al. 2015, *A&A*, **580**, A31  
 Hawkins, K., Jofré, P., Heiter, U., et al. 2016, *A&A*, **592**, A70  
 Heiter, U., Jofré, P., Gustafsson, B., et al. 2015, *A&A*, **582**, A49  
 Hill, J., Green, R. F., Ashby, D. S., et al. 2012, *SPIE*, **8444**-1  
 Hinkle, K., Wallace, L., Valenti, J., & Harmer, D. 2000, *Visible and Near Infrared Atlas of the Arcturus Spectrum 3727–9300 \AA (San Francisco: ASP)  
 Hubrig, S., Plachinda, S. I., Hüsch, M., & Schröder, K. P. 1994, *A&A*, **291**, 890  
 Ilyin, I. 2000, PhD Thesis, Univ. of Oulu  
 Jofré, P., Heiter, U., Soubiran, C., et al. 2014, *A&A*, **564**, A133  
 Jofré, P., Heiter, U., Soubiran, C., et al. 2015, *A&A*, **582**, A81  
 Jovanovic, M., Weber, M., & Allende-Prieto, C. 2013, *Publ. Astron. Obs. Belgrade*, **92**, 169  
 Keenan, P. C., & Hynek, J. A. H. 1945, *ApJ*, **101**, 265  
 Keenan, P. C., & McNeil, R. C. 1989, *ApJS*, **71**, 245*

<sup>2</sup> <https://pepsi.aip.de>

- Kim, K. M., Mkrtichian, D. E., Lee, B. C., Han, I., & Hatzes, A. P. 2006, *A&A*, **454**, 839
- Kjeldsen, H., Bedding, T. R., Baldry, I. K., et al. 2003, *AJ*, **126**, 1483
- Kumar, Y. B., Reddy, B. E., & Lambert, D. L. 2011, *ApJ*, **730**, L12
- Kupka, F., et al. (VAMDC Collaboration) 2011, *Baltic Astron.*, **20**, 503
- Kurucz, R. L., Furenlid, I., Brault, J., & Testerman, L. 1984, Solar Flux Atlas from 296 to 1300 nm. (Sunspot: National Solar Observatory)
- Lebzelter, T., Heiter, U., Abia, C., et al. 2012, *A&A*, **547**, A108
- Lee, B.-C., Han, I., Park, M.-G., et al. 2014, *A&A*, **566**, A67
- Lee, B. C., Han, I., Park, M.-G., et al. 2016, *AJ*, **151**, 106
- Luck, R. E. 2014, *AJ*, **147**, 137
- Luck, R. E., & Heiter, U. 2007, *AJ*, **133**, 2464
- Mack, C. E. III, Strassmeier, K. G., Ilyin, I., Schuler, S. C., & Spada, F. 2018, *A&A*, **612**, A46
- Mayor, M., Pepe, F., Queloz, D., et al. 2003, *The Messenger*, **114**, 20
- McArthur, B. E., Benedict, F. G., Henry, G. W. et al. 2014, *ApJ*, **795**, 41
- Meléndez, J., Asplund, M., Gustafsson, B., & Yong, D. 2009, *ApJ*, **704**, L66
- Molaro, P., Esposito, M., Monai, S. et al. 2013, *A&A*, **560**, A61
- Morgan, W. W. 1972, *AJ*, **77**, 35
- Morgan, W. W., & Roman, N. G. 1950, *ApJ*, **112**, 362
- Nassau, J. J., & MacRae, D. A. 1949, *ApJ*, **110**, 478
- Nilsson, H., Zang, Z. G., Lundberg, H., Johansson, S., & Nordström, B. 2002a, *A&A*, **382**, 368
- Nilsson, H., Ivarsson, S., Johansson, S., & Lundberg, H. 2002b, *A&A*, **381**, 1090
- Norlen, G. 1973, *Phys. Scr.*, **8**, 249
- Paletou, F., Böhm, T., Watson, V., & Trouilhet, J.-F. 2015, *A&A*, **573**, A67
- Palmer, B. A., & Engleman, R. 1983, *Atlas of the Thorium Spectrum* (Los Alamos: National Laboratory)
- Probst, R. A., Wang, L., Doerr, H.-P. et al. 2015, *New J. Phys.*, **17**, 023048
- Reiners, A., Mrotzek, N., Lemke, U., Hinrichs, J., & Reinsch, K. 2016, *A&A*, **587**, A65
- Ryabchikova, T., Ryabtsev, A., Kochukhov, O., & Bagnulo, S. 2006, *A&A*, **456**, 329
- Sablowski, D. P., Weber, M., Woche, M., et al. 2016, *SPIE*, **99125H**
- Sennhauser, C., & Berdyugina, S. V. 2011, *A&A*, **529**, A100
- Siqueira Mello, C., Hill, V., Barbuy, B., et al. 2014, *A&A*, **565**, A93
- Smiljanic, R., Korn, A. J., Bergemann, M., et al. 2014, *A&A*, **570**, A122
- Soubiran, C., Le Campion, J.-F., Cayrel de Strobel, G., & Caillou, A. 2010, *A&A*, **515**, A111
- Strassmeier, K. G. 2009, *A&ARv*, **17**, 251
- Strassmeier, K. G., Weber, M., Granzer, T., & Järvinen, S. 2012, *Astron. Nachr.*, **333**, 663
- Strassmeier, K. G., Ilyin, I., Järvinen, A., et al. 2015, *Astron. Nachr.*, **336**, 324
- Strassmeier, K. G., Ilyin, I., & Steffen, M. 2018, *A&A*, **612**, A44
- Wallace, L., Hinkle, K. H., Livingston, W. C., & Davis, S. P. 2011, *ApJS*, **195**, 6
- Wickliffe, M. E., Lawler, J. E., & Nave, G. 2000, *J. Quant. Spectr. Rad. Transf.*, **66**, 363

## Appendix A: Detailed observing log

Table A.1. Log of individual spectra.

Star	MK	Individual-spectrum S/N						N	Date	Telescope
		I/404	II/450	III/508	IV/584	V/685	VI/825			
<i>Giants</i>										
32 Gem	A9 III	100	115	205	270	265	240	222 222	15Apr 10	LBT
HD 140283	F3 IV	140	210	290	450	480	490	222 224	15May 25	LBT
HD 122563	F8 IV	100	160	245	310	405	400	222 224	15Apr 10	LBT
$\eta$ Boo	G0 IV	400	440	600	800	750	450	233 36(10)	15Apr 9	LBT
$\zeta$ Her	G0 IV	...	...	260	...	640	...	003 030	16Apr 2	VATT
$\zeta$ Her	G0 IV	...	120	260	395	600	530	032 222	16Apr 3	VATT
$\zeta$ Her	G0 IV	...	140	295	...	650	540	011 011	16Apr 5	VATT
$\zeta$ Her	G0 IV	...	35	...	170	...	110	020 101	16Apr 7	VATT
$\zeta$ Her	G0 IV	...	70	...	250	...	...	020 200	16Apr 10	VATT
$\zeta$ Her	G0 IV	690	...	...	...	...	700	200 00(10)	16Jun 3	LBT
delta CrB	G3.5III	320	320	420	500	500	630	122 223	17Mar 3	LBT
$\mu$ Her	G5 IV	...	...	110	...	200	...	002 020	15May 29	VATT
$\mu$ Her	G5 IV	...	50	120	190	310	300	012 111	15May 30	VATT
$\mu$ Her	G5 IV	...	40	95	145	245	250	012 111	15Jun 1	VATT
$\mu$ Her	G5 IV	...	50	100	160	265	255	012 111	15Jun 2	VATT
$\mu$ Her	G5 IV	570	440	480	740	710	610	255 55(10)	16Jun 3	LBT
$\beta$ Boo	G8 III	...	300	395	500	600	...	0(10)(10)(10)(10)0	16Jun 4	LBT
$\beta$ Boo	G8 III	400	...	...	...	...	550	300 00(14)	16Jun 5	LBT
$\epsilon$ Vir	G8 III	230	...	...	...	...	500	300 008	15Apr 8	LBT
$\epsilon$ Vir	G8 III	...	70	125	185	280	330	063 333	15Apr 1	VATT
$\beta$ Gem	K0 IIIb	150	...	...	...	...	330	600 008	15Apr 8	LBT
$\beta$ Gem	K0 IIIb	...	50	185	125	425	...	033 330	15Apr 2	VATT
$\beta$ Gem	K0 IIIb	...	...	...	300	...	...	000 200	15Apr 3	VATT
$\beta$ Gem	K0 IIIb	...	70	...	230	...	500	060 303	15Apr 4	VATT
HD 107328	K0 IIIb	190	250	500	650	900	990	343 436	15May 23	LBT
$\alpha$ UMa	K0 III	230	...	...	...	...	370	300 006	15Apr 9	LBT
$\alpha$ UMa	K0 III	...	75	170	300	440	400	063 333	15Apr 6	VATT
$\alpha$ Ari	K1 IIIb	700	...	...	900	...	...	300 800	15Sep 27	LBT
$\alpha$ Ari	K1 IIIb	...	260	300	...	570	650	066 066	15Nov. 20	LBT
$\alpha$ Boo	K1.5 III	250	500	...	350	...	500	630 509	15Apr 8	LBT
$\alpha$ Boo	K1.5 III	...	105	245	420	620	...	034 340	15Apr 2	VATT
$\alpha$ Boo	K1.5 III	...	110	...	...	...	650	080 008	15Apr 3	VATT
$\alpha$ Boo	K1.5 III	60	...	...	...	350	...	300 0(21)0	15Apr 5	VATT
$\alpha$ Boo	K1.5 III	75	...	...	...	450	...	300 0(21)0	15Apr 6	VATT
7 Psc	K2 III	170	295	550	660	1000	900	233 334	15Nov 20	LBT
$\mu$ Leo	K2 III	80	...	...	...	...	300	200 00(10)	15Apr 8	LBT
$\mu$ Leo	K2 III	200	210	300	430	530	550	234 346	15Apr 9	LBT
$\gamma$ Aql	K3 II	...	...	85	...	210	...	001 010	15May 7	VATT
$\gamma$ Aql	K3 II	...	150	360	570	900	845	021 111	16May 24	VATT
$\gamma$ Aql	K3 II	...	150	330	320	755	890	021 111	16May 26	VATT
$\gamma$ Aql	K3 II	...	150	350	440	800	935	021 111	16May 28	VATT
$\gamma$ Aql	K3 II	...	160	360	500	870	960	021 111	16May 29	VATT
$\gamma$ Aql	K3 II	...	100	250	315	590	340	021 111	16May 30	VATT
$\gamma$ Aql	K3 II	410	...	...	...	...	950	200 006	16Jun 5	LBT
$\beta$ UMi	K4 III	160	200	400	560	900	750	433 33(12)	15May 23	LBT
$\beta$ UMi	K4 III	...	...	50	...	150	...	003 0(21)0	15Apr 7	VATT
$\alpha$ Tau	K5 III	...	180	210	695	650	1200	063 335	15Sep 19	VATT
$\alpha$ Tau	K5 III	480	500	920	600	1300	1400	355 955	16Oct 1	LBT
$\mu$ UMa	M0 III	...	50	80	190	300	300	064 343	15Apr 4	VATT
$\mu$ UMa	M0 III	160	...	...	...	...	400	300 00(12)	15Apr 9	LBT
$\mu$ UMa	M0 III	...	140	340	420	730	...	032 420	17Mar 3	LBT
$\gamma$ Sge	M0 III	...	50	100	210	355	...	011 110	15May 27	VATT
$\gamma$ Sge	M0 III	...	...	145	...	450	...	001 010	15May 28	VATT
$\gamma$ Sge	M0 III	...	40	50	205	245	...	011 110	15May 29	VATT
$\gamma$ Sge	M0 III	...	50	95	200	340	...	011 110	15May 30	VATT
$\gamma$ Sge	M0 III	...	40	95	200	350	...	011 110	15Jun 1	VATT
$\gamma$ Sge	M0 III	...	40	95	200	340	...	011 110	15Jun 2	VATT
$\gamma$ Sge	M0 III	...	60	110	290	335	525	041 222	15Sep 19	VATT
$\gamma$ Sge	M0 III	...	63	120	220	310	500	042 222	15Sep 21	VATT
$\gamma$ Sge	M0 III	...	...	260	...	500	...	002 020	15Sep 25	LBT
$\gamma$ Sge	M0 III	340	...	...	...	...	850	200 00(13)	16Jun 3	LBT
$\alpha$ Cet	M1.5 IIIa	480	...	...	900	...	...	300 900	15Sep 27	LBT
$\alpha$ Cet	M1.5 IIIa	...	190	400	...	750	980	026 062	15Nov 20	LBT

Notes. As for Table 1. Date is the night of observation in UT (e.g., 16Apr means April 2016).

Table A.1. Continued.

Star	MK	Individual-spectrum S/N						<i>N</i>	Date	Telescope
		I/404	II/450	III/508	IV/584	V/685	VI/825			
<i>Dwarfs</i>										
$\alpha$ CMa	A1 V	800	590	720	740	620	420	111 111	16 Oct 1	LBT
HD 84937	F2 V	35	75	120	110	150	75	222 222	15Apr 2	LBT
HD 84937	F2 V	66	80	...	100	...	180	130 301	17Mar 3	LBT
$\sigma$ Boo	F4 V	...	...	165	...	390	...	003 030	16Apr 2	VATT
$\sigma$ Boo	F4 V	...	85	170	235	360	295	021 111	16Apr 3	VATT
$\sigma$ Boo	F4 V	...	85	180	285	380	305	021 111	16Apr 4	VATT
$\sigma$ Boo	F4 V	...	60	...	195	...	...	020 200	16Apr 10	VATT
$\sigma$ Boo	F4 V	...	115	...	...	...	390	010 001	16May 25	VATT
$\sigma$ Boo	F4 V	...	100	...	...	...	380	010 001	16May 27	VATT
$\sigma$ Boo	F4 V	...	...	220	...	390	...	001 010	16May 29	VATT
$\sigma$ Boo	F4 V	...	115	...	...	...	380	010 001	16May 31	VATT
$\sigma$ Boo	F4 V	...	102	...	...	...	...	010 000	16Jun 2	VATT
$\sigma$ Boo	F4 V	460	...	...	...	...	650	200 006	16Jun 3	LBT
HD 49933	F5 V-IV	...	...	240	...	400	...	004 040	16Apr 11	LBT
HD 49933	F5 V-IV	280	320	500	600	670	510	122 222	16Oct 1	LBT
$\alpha$ CMi	F5 V-IV	...	120	225	350	500	430	0(12)6 666	15Apr 5	VATT
$\alpha$ CMi	F5 V-IV	280	...	...	...	...	310	500 008	15Apr 8	LBT
$\theta$ UMa	F7 V	...	110	215	330	485	445	042 222	16Apr 4	VATT
$\theta$ UMa	F7 V	...	80	160	230	300	300	042 222	16Apr 5	VATT
$\theta$ UMa	F7 V	...	80	200	220	430	360	042 222	16Apr 6	VATT
$\theta$ UMa	F7 V	...	96	170	265	390	...	022 220	16Apr 10	VATT
$\theta$ UMa	F7 V	120	...	...	...	...	260	100 001	16Apr 11	LBT
$\theta$ UMa	F7 V	450	...	...	...	...	500	200 006	16Jun 3	LBT
$\beta$ Vir	F9 V	225	...	...	...	...	350	200 007	15Apr 8	LBT
$\beta$ Vir	F9 V	...	55	95	120	175	...	043 430	15Apr 3	VATT
$\beta$ Vir	F9 V	...	50	...	...	...	160	030 003	15Apr 5	VATT
HD 22879	F9 V	...	330	410	590	570	...	021 210	15Sep 27	LBT
HD 22879	F9 V	205	...	...	...	...	420	100 001	16Oct 1	LBT
HD 189333	F9 V	88	170	245	230	290	340	111 111	16Oct 1	LBT
HD 52265	G0 V	...	...	97	...	168	80	001 011	16Apr 5	VATT
HD 52265	G0 V	...	...	30	...	76	50	011 011	16Apr 6	VATT
HD 159222	G1V	210	260	375	500	560	530	232 323	16Jun 5	LBT
16 Cyg A	G1.5 V	180	215	410	540	630	500	122 223	15May 25	LBT
Sun	G2 V	...	...	...	...	...	...	444 446	15Sep 24	SDI
HD 101364	G2 V	...	...	80	...	110	...	003 030	15Apr 8	LBT
HD 101364	G2 V	55	110	145	185	200	185	333 333	15Apr 10	LBT
HD 82943	G2 V	50	120	160	200	220	160	322 223	15Apr 2	LBT
18 Sco	G2 V	180	250	450	550	700	690	233 333	15May 23	LBT
18 Sco	G2 V	270	...	...	450	590	...	200 440	15May 24	LBT
51 Peg	G2.5 V	240	380	550	640	810	700	344 445	15Nov 20	LBT
16 Cyg B	G3 V	...	390	420	650	650	650	022 223	15May 25	LBT
16 Cyg B	G3 V	220	...	...	...	670	...	100 040	15Sep 27	LBT
70 Vir	G4 V	250	380	680	810	1000	900	222 224	15May 25	LBT
$\mu$ Cas	G5 V	480	420	700	810	1080	1100	122 222	15Sep 27	LBT
HD 103095	G8 V	105	145	220	275	325	325	233 433	15Apr 10	LBT
$\tau$ Cet	G8.5 V	...	66	165	...	385	380	011 011	15Sep 20	VATT
$\tau$ Cet	G8.5 V	450	...	...	540	700	...	400 380	15Sep 27	LBT
$\tau$ Cet	G8.5 V	...	...	184	...	390	...	001 010	15Nov 28	VATT
$\tau$ Cet	G8.5 V	...	...	150	...	400	...	001 010	15Nov 29	VATT
$\tau$ Cet	G8.5 V	...	...	138	...	398	...	001 010	15Nov 30	VATT
$\tau$ Cet	G8.5 V	...	...	191	...	537	...	001 010	15Dec 1	VATT
$\tau$ Cet	G8.5 V	...	...	153	...	435	...	001 010	15Dec 2	VATT
$\tau$ Cet	G8.5 V	...	...	230	...	580	...	001 010	15Dec 3	VATT
$\tau$ Cet	G8.5 V	...	...	225	...	574	...	001 010	15Dec 4	VATT
$\tau$ Cet	G8.5 V	...	...	101	...	237	...	001 010	15Dec 5	VATT
$\tau$ Cet	G8.5 V	...	...	210	...	520	...	001 010	15Dec 6	VATT
$\tau$ Cet	G8.5 V	...	370	530	750	...	710	055 505	16Oct 1	LBT
$\epsilon$ Eri	K2 V	...	...	185	...	475	...	001 010	15Sep 24	VATT
$\epsilon$ Eri	K2 V	540	450	630	800	1100	1000	155 555	16Oct 1	LBT
HD 192263	K2 V	172	209	310	330	450	480	122 222	16Jun 6	LBT
HD 128311	K3 V	45	100	130	180	210	200	322 223	15Apr 8	LBT
HD 82106	K3 V	50	80	140	195	220	210	213 132	15Apr 1	LBT
61 Cyg A	K5 V	...	...	...	...	...	...	002 020	15May 25	LBT
61 Cyg A	K5 V	240	520	700	900	1000	850	122 334	15Sep 27	LBT
61 Cyg B	K7 V	176	230	440	550	910	720	122 224	15Sep 27	LBT